https://doi.org/10.5194/egusphere-2026-400
Preprint. Discussion started: 11 February 2026

Assessing Earth's Skin Temperature Trends: Consistent Signals from IASI, MODIS, CCI and ERA5

Sarah Safieddine[1*], Selviga Sinnathamby[1], Juliette Hadji-Lazaro[1], Marie Doutriaux-Boucher[2], Darren Ghent[3], Simon Whitburn[4,5], Lieven Clarisse[4], and Cathy Clerbaux[1,4]

[1] LATMOS/IPSL, Sorbonne Université, UVSQ, CNRS, Paris, France
[2] European Organisation for the Exploitation of Meteorological Satellites (EUMETSAT), Darmstadt, Germany
[3] National Centre for Earth Observation (NCEO), University of Leicester, UK
[4] Université libre de Bruxelles (ULB), Spectroscopy, Quantum Chemistry and Atmospheric Remote Sensing (SQUARES), Brussels, Belgium
[5] Royal Meteorological Institute of Belgium (KMI-IRM), Atmospheric Composition, Measurements and Modelling division (ACM²), Brussels, Belgium

Correspondence to: Sarah Safieddine (sarah.safieddine@latmos.ipsl.fr)

Abstract. Earth's skin temperature (Tskin), i.e. land and sea surface temperature (LST and SST), directly reflects surface–atmosphere energy exchanges and is an Essential Climate Variable (ECV). Yet it remains less exploited than near-surface air temperature in climate monitoring. Here, we intercompare and assess the capability of several infrared sounders and Tskin products to monitor climate variability during morning and evening overpasses from a multi-sensor perspective over 2008–2022. Two Infrared Atmospheric Sounding Interferometer (IASI) satellite products are analysed: the EUMETSAT all-sky Climate Data Record (IASI-CDR) (all-sky) and a newly developed clear-sky neural-network product (IASI-NN). These IASI products are compared with the Moderate Resolution Imaging Spectroradiometer MODIS Terra Land Surface Temperature (LST) (v6.1), ESA LST CCI (v3.00), and ERA5 skin temperature.

Over land, daytime global means agree within ~2 K across datasets, but LST CCI is consistently higher, and deseasonalised anomalies are highly consistent, except for LST CCI, which exhibits sensor-transition discontinuities. At night, MODIS shows a prevalent cold bias relative to all other products. Over the ocean, inter-dataset biases between IASI and ERA5 generally remain below 1 K. Trend analyses reveal robust warming in Tskin since 2008 across the different datasets, while significant regional cooling is observed over India (daytime) and parts of central/eastern Africa, and in in the southeastern Pacific associated with the Humboldt upwelling system.

1 Introduction

Near-surface air temperature is routinely monitored and assimilated in meteorological reanalyses, providing a foundation for climate analysis, but it remains an indirect proxy of surface–atmosphere exchanges. In contrast, land and sea surface temperatures (LST and SST), collectively referred to as Earth's skin temperature (Tskin), directly capture the thermal state of

https://doi.org/10.5194/egusphere-2026-400
Preprint. Discussion started: 11 February 2026

the Earth's uppermost surface layer and its interaction with the atmosphere. Despite being recognized as Essential Climate Variables (Guillevic et al., 2018), Tskin measurements are still underexploited in climate and urban applications.

Tskin responds immediately to changes in radiative forcing, land use, and atmospheric conditions. It is therefore a key variable for studying Earth's energy balance (Hulley et al., 2019), surface convection, drought monitoring, land-use and land-cover changes, and urban heat islands (Rhee et al., 2010; Zhou et al., 2003). Owing to its direct sensitivity to surface–atmosphere interactions, Tskin serves as a reliable tracer of climate variability.

For cloud-free scenes, neglecting atmospheric absorption, Tskin can be retrieved from radiances using the inverse of Planck's law (Eq. 1):

$$T = \frac{hcx}{k\,log\left(\frac{2\epsilon hc^2x^3}{L(x)}+1\right)} \qquad \text{(Eq.1)}$$

Where: x is the wavenumber in cm^{-1}, L is the radiance $W \cdot m^{-2} \cdot sr^{-1} \cdot (cm^{-1})^{-1}$, k is Boltzmann's constant = 1.3806×10^{-23} $J \cdot K^{-1}$, h is Planck's constant = 6.6262×10^{-34} J·s, c is the speed of light in vaccum= 2.9979×10^{10} $cm \cdot s^{-1}$, and ϵ is the surface emissivity. In this study, we compare and evaluate several Tskin and/or LST/SST products to assess their spatial–temporal consistency and their ability to capture climate variability. Specifically, we analyse:

- the Moderate Resolution Imaging Spectroradiometer (MODIS) Terra LST product,
- the latest European Space Agency (ESA) Climate Change Initiative LST product (LST CCI v3.00, released August 2025),
- the European Centre for Medium-Range Weather Forecasts (ECMWF) ERA5 reanalysis skin temperature, and
- two Tskin products from the Infrared Atmospheric Sounding Interferometer (IASI):
  (i) the EUMETSAT (European Organisation for the Exploitation of Meteorological Satellites) all-sky Climate Data Record (IASI-CDR), and
  (ii) a newly developed clear-sky near-real-time neural-network product (IASI-NN).

This study offers two important advances. First, it provides the first global intercomparison that brings together the newly developed IASI neural-network product (IASI-NN), the EUMETSAT IASI CDR (IASI-CDR), and the most recent ESA LST CCI v3.00 dataset. Second, it is the first analysis to examine day- and night-time Tskin trends consistently across all these observing systems, allowing us to assess the diurnal fingerprint of climate change from a multi-sensor perspective. In the following, "Tskin" refers to either land surface temperature (LST) or sea surface temperature (SST), depending on and if the quantity is provided by each dataset. Section 2 introduces the datasets, Section 3 presents their intercomparison, Section 4 assesses climate trends and their spatial patterns, and Section 5 summarizes the main findings and discusses their implications.

2 Methods

For consistency between datasets, the satellites orbits are all between 9:30 and 10:30 am and pm. Reanalysis data is chosen at 10 am.

2.1 MODIS LST temperature products

The Land Surface Temperature product is the 6.1 version, developed by NASA's Land Processes Distributed Active Archive Center (LP DAAC). The data is extracted at a 0.05-degree latitude/longitude grid, and regridded to 1x1 grid size for discussion and analysis. The dataset provides monthly LST and emissivity data derived from MODIS, carried aboard the Terra (Wan, et

https://doi.org/10.5194/egusphere-2026-400
Preprint. Discussion started: 11 February 2026

al., 2021) satellite. NASA's Terra is a sun-synchronous, polar orbiting satellite in a morning orbit, with equator crossing times of approximately 10:30 am and 10:30 pm (local time) in descending and ascending modes respectively. In this work, we focus on the Terra satellite because of its close crossing time to the other datasets listed hereafter. Terra (and Aqua) have been drifting to an earlier equatorial crossing time since 2020. NORAD (North American Aerospace Defense Command) data (not shown here) suggests that by the end of 2022, the equatorial crossing time was around 10:11 pm, for a total of 19-minute drift. The ~19-minute drift remains small relative to the monthly sampling used in this study and should not introduce overpass-condition changes capable of biasing the comparisons between the different datasets.

2.2 ESA Land Surface Temperature Climate Change Initiative (LST CCI)

To complement our analysis, we use the ESA LST CCI Monthly Multisensor Infrared (IR) Low Earth Orbit Land Surface Temperature Level 3 Supercollated (L3S) global product, version 3.00 (Ghent et al., 2025), which is online since August 2025. Daytime and nighttime temperatures are provided in separate files, corresponding to local solar times of 10:00 am and pm, respectively. The instruments contributing to the time series used in this study are AATSR (Advanced Along-Track Scanning Radiometer, until March 2012), MODIS Terra (from April 2012 to November 2018), and SLSTR-B (the Sea and Land Surface Temperature Radiometer on Sentinel 3B, starting in December 2018). The MODIS brightness temperature data was also intercalibrated against IASI. For consistency, a common algorithm is applied for LST retrieval across all instruments. In addition, an adjustment is made to account for the half-hour difference in the satellites' equatorial crossing times (Ghent et al., 2025). Data are retrieved at a 0.01-degree latitude/longitude grid, that we regridded to 1x1 grid size for discussion and analysis.

2.3 ERA5 Tskin

We use the Tskin variable from the ERA5 reanalysis (Hersbach et al., 2020), produced by ECMWF, which is framed within the Copernicus Climate Change Service (C3S) of the European Commission. ERA5 datasets are at $0.25^{\circ} \times 0.25^{\circ}$ resolution (native horizontal resolution of ERA5 is ~31km), that are regridded to a 1° x1° grid size for the study. Tskin is a diagnostic (non-prognostic) variable of ERA5 that is calculated at each time step based on surface energy balance equations. Since Tskin is diagnostic, it is not a primary variable directly predicted by the model (unlike near surface temperatures for example). Hourly averages are computed for each month of the year and are then converted to local time by calculating the time zone offset based on the longitude (15° = 1 hour). Our analysis does not account for daylight saving time. This is consistent with satellite local-solar-time definitions, as polar-orbiting instruments such as IASI maintain fixed solar crossing times (e.g., 09:30/21:30), independent of civil time zones.

2.4 IASI climate data record Tskin product from EUMETSAT

IASI (Clerbaux et al., 2009) is a Fourier transform spectrometer and data are available from three instruments onboard of Metop-A, -B and -C satellites launched in 2006 (end of life in October 2021), 2012, 2018, respectively. Each IASI instrument provides more than 1.2 million radiance spectra per day with a footprint on the ground of 12 km diameter at nadir, and a local crossing time of 9:30 AM and 9:30 PM. IASI has exceptional spectral and radiometric stability making a reference instrument (Kilymis et al., 2025). IASI Tskin data are officially distributed by EUMETSAT and is derived from IASI radiances but also relies on two microwave instruments onboard Metop satellites—the Microwave Humidity Sounder (MHS) and the Advanced Microwave Sounding Unit-A (AMSU-A)—particularly for cloudy scenes. Several updates have been made to the processing algorithm over time (Bouillon et al., 2020), which has been relatively stable since 2016, making the product operational but not homogeneous over time. To this end, EUMETSAT provided an all-sky climate data record (IASI-CDR) Tskin product. In this work we use the latest CDR version, 1.1, which is a homogeneously reprocessed dataset from the surface to the top of the atmosphere (EUMETSAT, 2022). The reprocessed temperatures were computed with a piecewise linear regression cube ($PWLR^3$) algorithm, using all IASI observations as input (clear and cloudy scenes). It is a fast and accurate statistical retrieval scheme that exploits the synergy between microwave (MHS, and AMSU) and infrared measurements. $PWLR^3$ is a machine learning algorithm trained with real satellite observations paired with the best correlative representation of the Earth system. The CDR includes four surface parameters (surface pressure, surface air temperature, surface air dew point temperature, and surface skin temperature) as well as the atmospheric profiles of temperature and humidity. Only surface skin temperature is used in this work. The training set used for the algorithm in this CDR is composed of three variables from the European Reanalysis (ERA5): temperature, humidity and ozone, provided at 137 model levels (Hersbach et al., 2020). It uses 96 days of data, i.e., 4 days (1st, 8th, 15th and 22nd) of each month for 2 years in 2015 and 2016. In total, the training set is made up of more than 120 million IASI fields of view. The algorithm defines different observation classes based on the IASI observations and auxiliary information (e.g. surface type and elevation). Then, for each observation class, a linear regression is performed from the IASI/AMSU-A/MHS observation to retrieve the required geophysical parameters.

2.5 IASI clear sky neural network Tskin

The IASI Neural Network (IASI NN) Tskin product used in this study is a clear-sky retrieval based on an information-content channel selection and a neural-network architecture. It is an updated version of the product validated by Safieddine et al. (2020). Surface temperature is derived using 87 window-region channels (750–950 cm^{-1}), reduced from 100 in the first version by removing channels sensitive to carbon dioxide (CO_2) to improve long-term stability. The list of channels is provided in the Appendix.

A second key update is the use of the EUMETSAT Tskin product from 2021 as the training target, replacing ERA5, as was done in Safieddine et al. (2020). This allows the NN to emulate an operational optimal-estimation surface temperature directly derived from IASI and ensures consistency over the entire mission.

2.5.1. Accounting for monthly and interannual emissivity variability

Over land, emissivity information is included as auxiliary input using the CAMEL (Combined ASTER, Advanced Spaceborne Thermal Emission and Reflection Radiometer, and MODIS Emissivity over Land) dataset. CAMEL merges the MODIS reference emissivity database (University of Wisconsin–Madison) with the ASTER GEDv4 emissivity dataset (Jet Propulsion Laboratory, JPL). It provides global coverage at 5 km resolution with monthly means across 13 spectral bands (3.6–14.3 µm). Four of these bands (10.6, 10.8, 11.3 and 12.1 µm), located within the spectral window relevant for Tskin retrievals, are incorporated into the NN input over land surfaces. The trends in emissivities are shown in the supplement, Figure S1. Across all four TIR channels, CAMEL exhibits predominantly negative emissivity trends**,** with spatially coherent patterns. Although the magnitude of these trends is small (>-0.1%/year), their persistence across channels suggests a systematic signal rather than random noise. The trends in emissivities will therefore affect the Tskin trends and are a necessary input to the Tskin retrievals. Other auxiliary variables were included following extensive testing: longitude and latitude (rounded to the nearest degree) and the field-of-view (pixel number from 1 to 120, with pixels 57–64 near nadir). The full set of input and target variables is summarised in Table 1.

https://doi.org/10.5194/egusphere-2026-400
Preprint. Discussion started: 11 February 2026

Table 1. Inputs and target variables for neural network training.
Total features/inputs: 90 over sea and 94 over land. Target variable: EUMETSAT Tskin.

Sea	Land
Longitudes	Longitudes
Latitudes	Latitudes
87 radiance channels (scaled $\times 1e^5$)	87 radiance channels (scaled $\times 1e^5$)
Pixel number	Pixel number
–	Four CAMEL emissivity channels
Target: EUMETSAT Tskin	**Target: EUMETSAT Tskin**

The dataset was split into training (70%), validation (9%) and test (21%) subsets. Hyperparameters were tuned with a batch size of 100 and a learning rate of 10^{-3} using the Adam optimizer. Training was performed for 200 epochs over the sea and 400 epochs over the land, reflecting the slower convergence behaviour of the latter. To ensure consistent scaling across features, a TensorFlow normalization layer was applied to normalize inputs to zero mean and unit variance.

To improve clear-sky detection, this version uses the cloud mask developed by Whitburn et al. (2022). This IASI-derived deep-learning cloud product is explicitly designed to be insensitive to CO_2 variability, enhancing long-term climate stability. Its performance has been validated against MODIS and AVHRR (Advanced Very High-Resolution Radiometer), showing improved accuracy across a wide range of atmospheric and surface conditions.

2.5.2 IASI measurement periods and satellites used

The two IASI-based Tskin datasets (NN and CDR) cover the following periods and instruments:

- July 2007 – January 2013: Metop-A (only satellite in orbit)
- February 2013 – December 2017: Metop-A + Metop-B (Metop-B available from 20 February 2013)
- January 2018 onward: Metop-B only (Metop-A orbit drift beginning July 2017 affected its equatorial crossing time, progressively influencing Tskin retrievals until end of life in 2021)

Since the EUMETSAT CDR does not include Metop-C for the years 2020–2022, Metop-C is not used in this study.

3 Cross-Platform Assessment of Surface Temperature Products

The study period considered here follows the availability of IASI, whose first operational data date from July 2007. We present in this section the intercomparison up to 2023 for all datasets (except for the IASI CDR which ends in 2022). All datasets are regridded onto a 1° × 1° grid and averaged monthly. Spatial means are weighted by the cosine of latitude to account for grid-cell area. We note that day/night notion reflects the morning/evening orbit for MODIS (at 10:30 am/pm) and IASI (around 9:30 am/pm), the combined morning orbit for the CCI satellite products (at 10 am/pm), and the 10 am/pm local time temperature product from ERA5 (Sect. 2).

3.1 Land Surface Temperature Analysis

We show in Figure 1, the global averages of LST (upper panels), and the deseasonalised anomaly (lower panels) from the 5 datasets used in this study (MODIS, CCI, ERA5, IASI CDR, IASI NN), during the day (left) and the night (right). For the Tskin, i.e., land + sea datasets (ERA5, IASI CDR et IASI NN), a sea mask is applied based on MODIS data.

https://doi.org/10.5194/egusphere-2026-400
Preprint. Discussion started: 11 February 2026

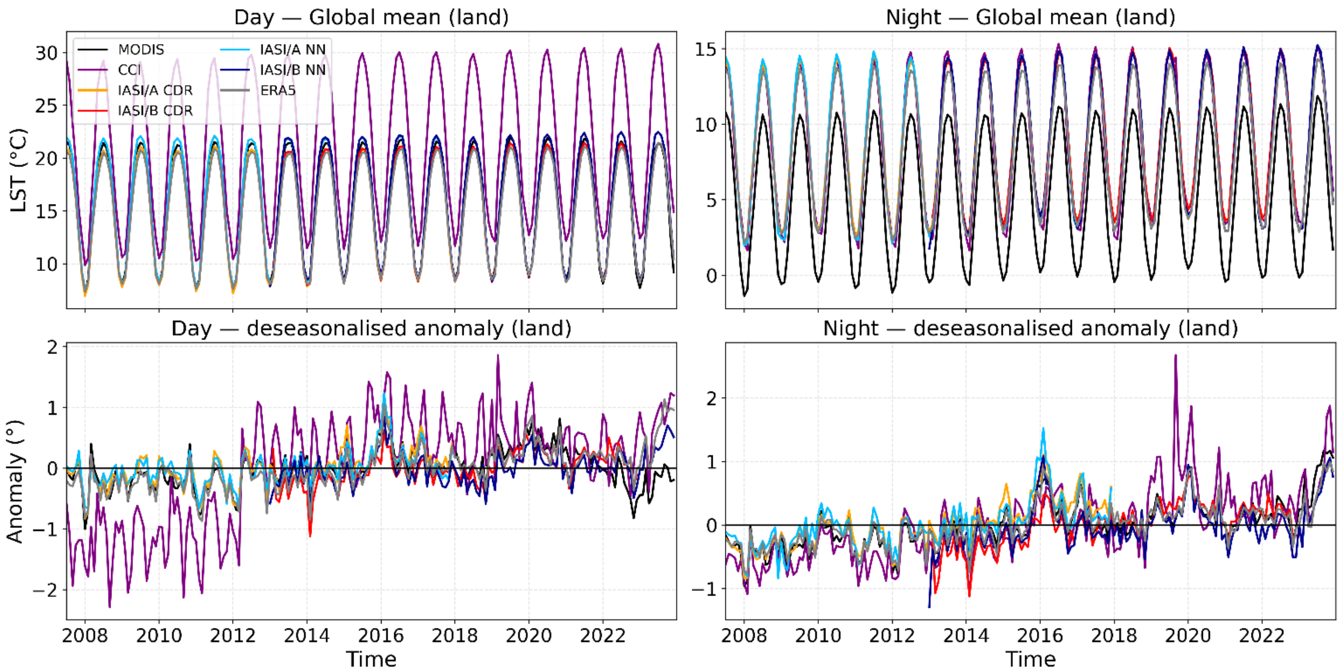

Figure 1. Global mean land surface temperature (LST) and deseasonalised anomalies for daytime (left) and nighttime (right). IASI Metop-A and Metop-B observations (IASI-A/B) are shown separately for the CDR and NN products. Global means are computed using cosine-latitude weighting.

During daytime, LST CCI is systematically warmer than the other datasets in the global mean (Figure 1, upper-left), yielding the highest LST values throughout most of the record. The deseasonalised anomalies display very good agreement among the different datasets, except for LST CCI. The shift from ASTER to MODIS/Terra in April 2012 is clearly visible in the anomaly time series, as is another shift in late 2018 (nighttime), corresponding to the introduction of SLSTR-B into the CCI dataset. This version of the CCI product has not yet been fully validated. Here we show that the addition of new sensors appears to affect the homogeneity of the LST time series.

At night, MODIS provides the lowest LST values. MODIS has the latest overpass time among the products considered, so we would expect that Tskin at 10:30 pm (Terra) to be lower than those at 9:30 pm (IASI) or at 10 pm (ERA5 and LST CCI). However, the magnitude of the MODIS cold bias cannot be explained solely by differences in equator-crossing times. To investigate this further, Figure 2 presents the spatial bias of MODIS with respect to the four other datasets. A pronounced nighttime cold bias is evident across all comparisons, including LST CCI, which includes MODIS data (but a distinct retrieval algorithm, see Sect. 2). Tan et al., 2021 validated MODIS LST against ground measurements and found a negative nighttime bias at most stations, with an average of −1.58 K. In high-latitude regions, cold biases have also been reported in the Arctic (Muster et al., 2015) and in Antarctica (Zhai et al., 2024), often linked to cloud-screening issues that affect the retrievals. Surface heterogeneity—including snow/ice, permafrost, and arid regions—can further influence MODIS LST (Hachem et al., 2012), though these challenges extend to other satellite products as well. In urban areas, nighttime MODIS LST retrievals have been shown to exhibit non-negligible errors (Yoo et al., 2022).
Figure 2 highlights the widespread MODIS negative (cold) bias over land at night. This suggests that the MODIS V6.1 LST product used here may exhibit a generalized nighttime cold bias that warrants further investigation. The daytime bias is smaller in magnitude, especially with LST CCI, and more spatially variable. When comparing MODIS to ERA5, the longitude

https://doi.org/10.5194/egusphere-2026-400
Preprint. Discussion started: 11 February 2026

"stripes" appears because of the local time conversion method (see Sect. 2). IASI-NN and MODIS agrees more in arid and ice-covered region likely because our neural-network product incorporates emissivity information derived (partly) from MODIS. Pronounced discrepancies between MODIS and ERA5 (as well as IASI-CDR trained with ERA5) over the Tibetan Plateau are consistent with known limitations of reanalyses in high-altitude and complex terrains (Khadka et al., 2022; Liu et al., 2024).

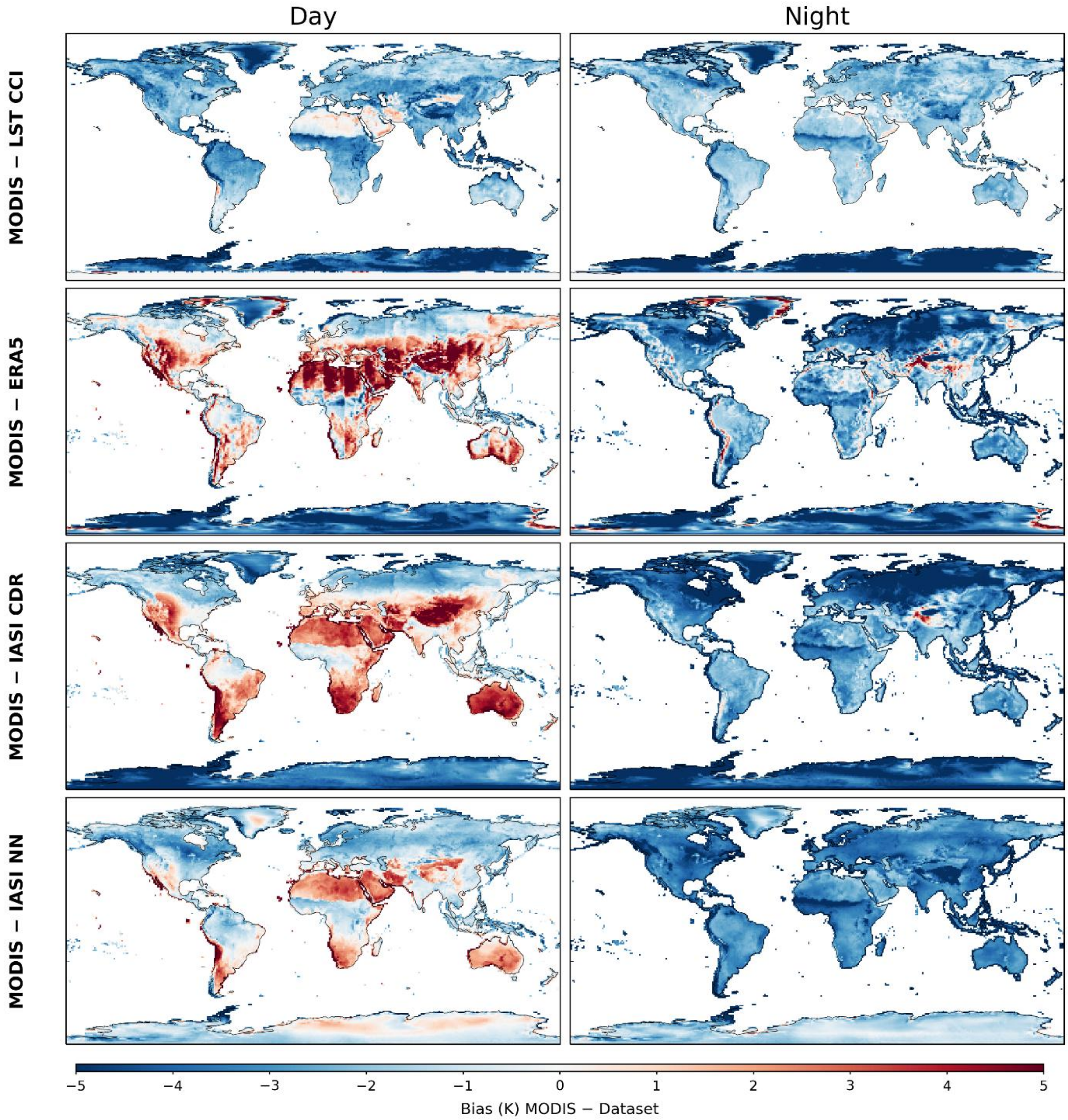

Figure 2. LST spatial bias averaged over the 2007-2022 period of MODIS during the day (left) and the night (right), with respect to LST CCI, ERA5, IASI-CDR and IASI-NN.

https://doi.org/10.5194/egusphere-2026-400
Preprint. Discussion started: 11 February 2026

We then show and compute the global averaged bias and root mean square errors (RMSE) over land areas, and between the different datasets in Figure 3. Both metrics were computed as spatially weighted averages using cos(latitude) weighting to account for the varying grid-cell area with latitude.

The datasets show good agreement during the day, with biases between the different products lower than 1 K (except for LST CCI, with biases between 1.8 and 2.6 in absolute value). RMSE values are globally high (> 4 K) except between ERA5 and IASI-CDR (< 2 K), and between IASI-NN and MODIS, ERA5 and IASI-CDR. The good agreement between IASI-CDR and ERA5 results from the fact that IASI-CDR algorithm is trained with ERA5 results. RMSE values are the highest for the LST CCI dataset during the day, representing the overall lower accuracy of this dataset. During the night, both the biases and RMSE are higher for MODIS with respect to the other datasets, as it was shown in Figures 1 and 2. The IASI-NN product shows biases below 1 K when compared with MODIS, ERA5, and the IASI-CDR dataset during the day, and has an average bias of 1.83 K relative to LST CCI. At night, IASI-NN agrees very well with the other products (< 1 K), except for MODIS, as shown and discussed previously. More generally, the IASI-NN product is the only one that is clear-sky. This can explain the positive bias with respect to other products (except MODIS).

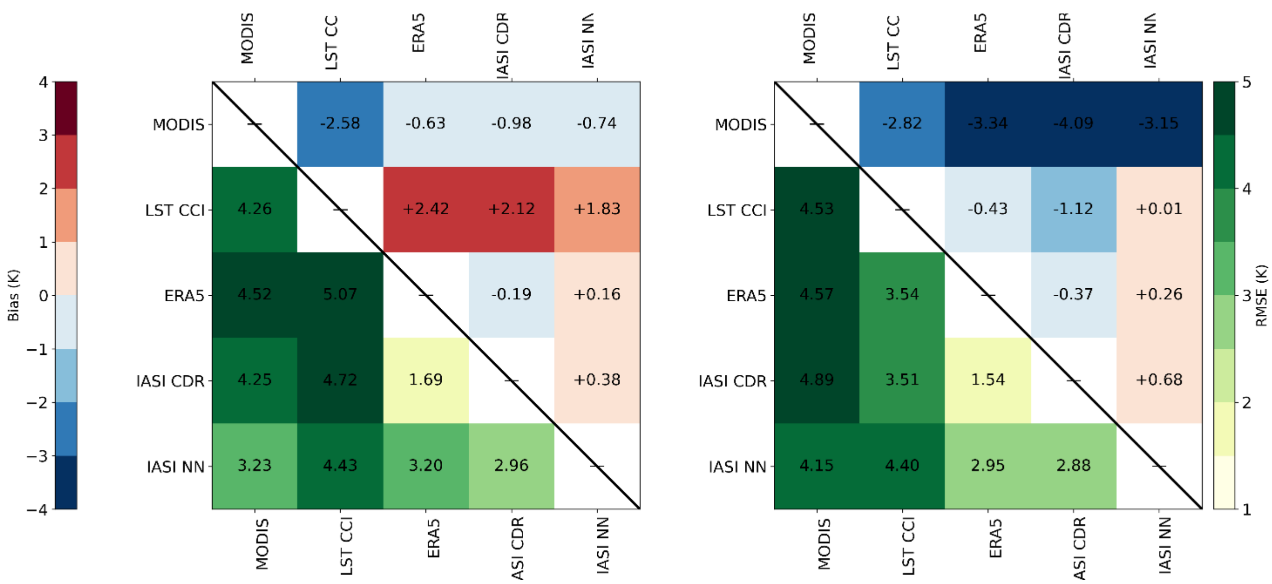

Figure 3. *Upper triangle (blue to red): global mean bias (row – column, y -x): Lower triangle (in yellow to green): root mean square error (RMSE) between the different pairs of LST datasets, for day (left) and night (right).*

3.2 Sea Surface Temperature Analysis

Figure 4 presents, similarly to Figure 1, the intercomparison of sea surface temperature (SST, or ocean Tskin) from the datasets providing this variable: ERA5 at 10 am/pm local time, the IASI-CDR, and IASI-NN (at 9:30 am/pm). The upper panel shows the global mean SST, and the lower panels display day- and night-time anomalies. MODIS data are used to mask land. The IASI-NN product represents clear-sky conditions, whereas the IASI CDR and ERA5 datasets are all-sky. As expected, IASI-NN therefore returns higher temperatures than the other two datasets. This behaviour was also seen over land (Figure 3) and appears here over the oceans, though with a smaller magnitude due to the ocean's higher heat capacity and reduced diurnal cycle. The latitude-weighted SST in Figure 4 consistently reflects this clear-sky warm bias. We also note that the y-axis ranges

https://doi.org/10.5194/egusphere-2026-400
Preprint. Discussion started: 11 February 2026

for both the time series and anomalies in Figure 4 are smaller than those in Figure 1 for LST, consistent with the lower variability of SST relative to land temperatures.

Biases between the datasets (Figure 5, with Metop-A and Metop-B averaged together) are much smaller than the land biases and very similar between daytime and nighttime, primarily because the ocean surface is more homogeneous. The biases and RMSE values shown on the panels are generally below 0.1 K and close to 1 K, respectively. A small positive bias appears in mid-latitudes which result from the difference of cloudy conditions between IASI-NN on the one hand and IASI-CDR and ERA5 on the other hand, while larger biases occur at high latitudes between IASI-NN and the both other datasets. The latter can be attributed to several factors: cloud detection challenges in polar regions (Whitburn et al., 2022), which can lead to residual cloud contamination in clear-sky retrievals; or reduced thermal contrast (temperature difference between Earth's surface and the air just above it) over cold oceans and sea-ice contamination, which decrease IASI sensitivity. Finally, once again, we find a close agreement between the IASI-CDR and ERA5 products as expected.

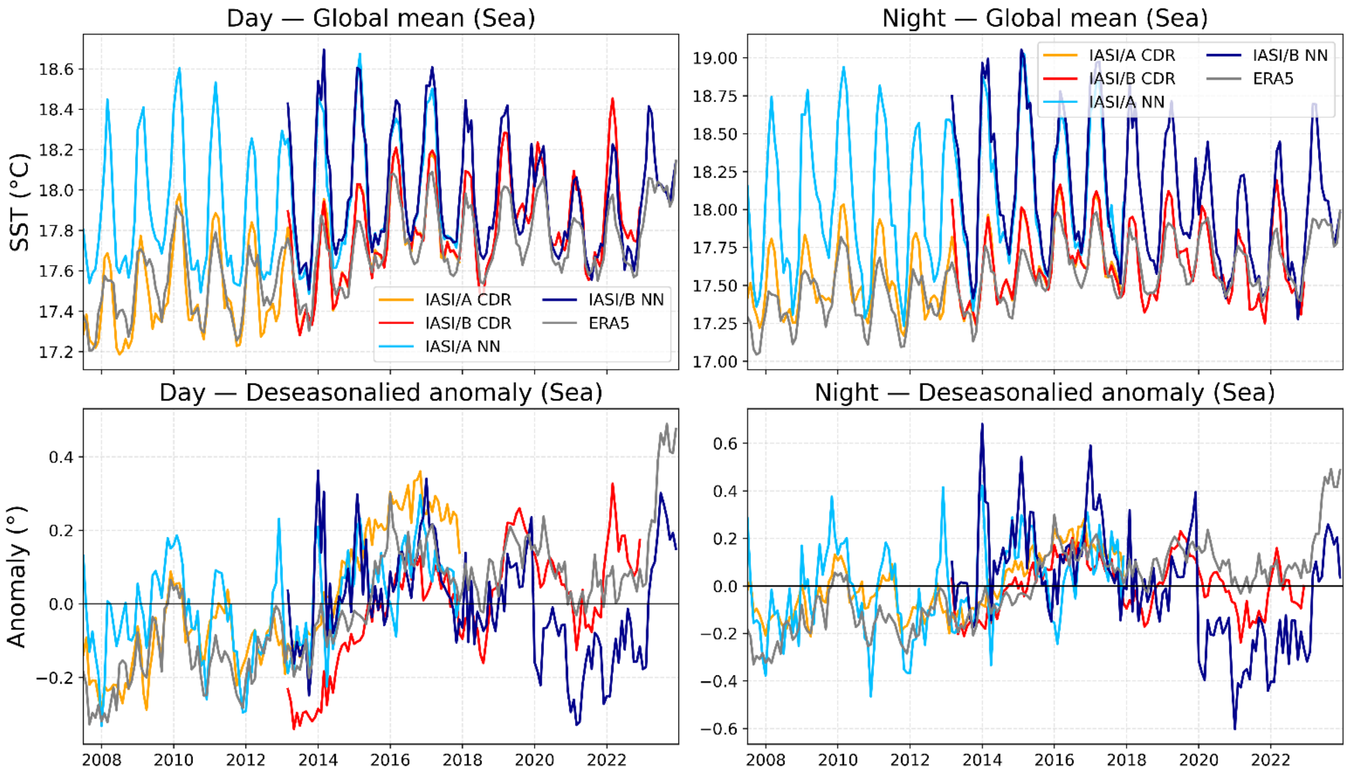

Figure 4. Upper panels: SST global mean during the day (left) and the night (right) for ERA5, IASI-CDR and IASI-NN. IASI data are separated between Metop A and Metop B. Lower panels: the deseasonalied anomaly of SST for the different products, during the day and night.

https://doi.org/10.5194/egusphere-2026-400
Preprint. Discussion started: 11 February 2026

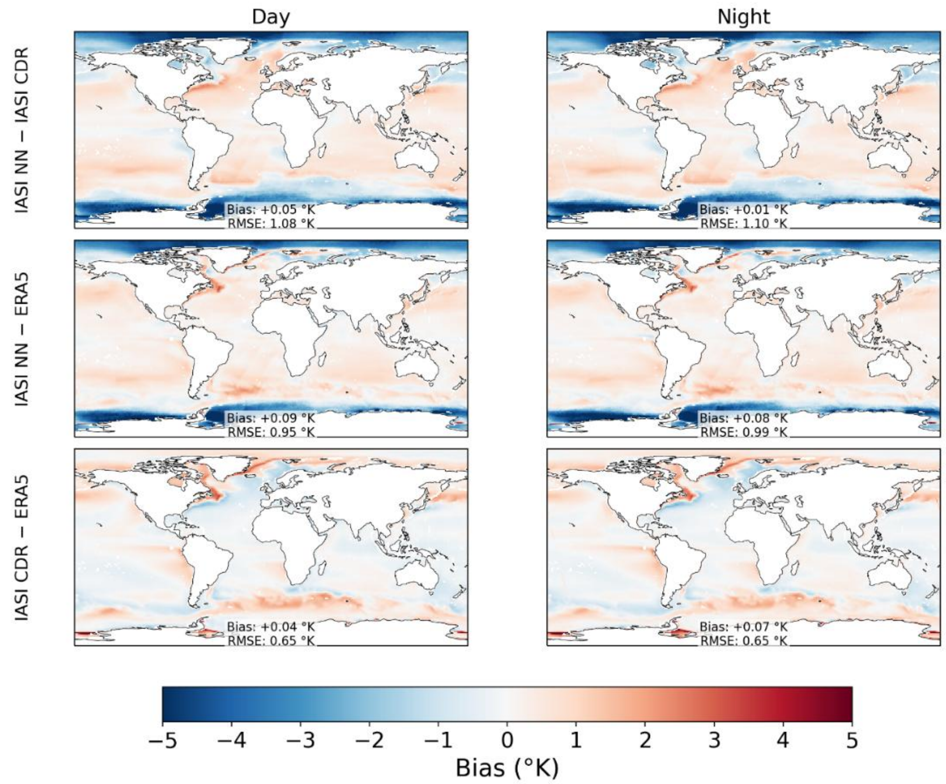

Figure 5. Spatial bias between IASI-NN, IASI-CDR, and ERA5 skin temperature over the ocean. Maps show the mean monthly bias for daytime (left column) and nighttime (right column) over the common period of the datasets [2007-2022]. All datasets were regridded to a common 1°×1° grid, and land points were masked using a MODIS-derived land mask. Global mean bias and RMSE (area-weighted by cos latitude) are indicated in each panel.

4 LST/Tskin trends over the period [Jan 2008- Dec 2022]

Daytime and nighttime LST/Tskin trends from the MODIS, CCI, ERA5, IASI CDR and IASI NN products for the period January 2008-December 2022 are shown in Figure 6. This period is selected as the IASI CDR product ends on the December 2022 (Sect. 2). Trends are computed using the Theil-Sen estimator on yearly deseasonalised averages of LST/Tskin in each grid cell (Sen, 1968; Theil, 1992). The Theil-Sen estimator is a robust trend detection method that calculates the slope between all pairs of data points and takes the median of these slopes. Positive (negative) trends are given in red (blue) shades and statistically significant trends are hatched. Trend significance is assessed using the Mann–Kendall test (Kedall, M. G., 1970; Mann, 1945), with trends considered significant when the p-value is below 0.05.

Spatial distribution of trends from the different datasets are generally closely correlated. As climate change has a diurnal signature at different times of the day (Safieddine et al., 2025), we notice that for the same dataset, day and night trends are different with daytime values more pronounced (positively or negatively). In the Northern Hemisphere (NH), over land and sea, all datasets show mostly positive trends with the strongest warming in Alaska and Siberia. Both observations and general circulation model projections suggest current and future significant temperature increases in Siberia consistent with the effects of Arctic amplification, with an increase mostly pronounced in central Siberia reaching 4°C over the past few decades (Masson-Delmotte, et al., 2021; Tchebakova et al., 2009). While most of the NH hemisphere has positive trends, India

https://doi.org/10.5194/egusphere-2026-400
Preprint. Discussion started: 11 February 2026

shows negative trends during the day, for all the datasets studied. In fact, aerosol emissions over India continued to increase in the past two decades (2000-2019) (Klimont et al., 2013; Wang et al., 2021). Aerosol optical depths retrievals from satellites show positive trends over the 2000-2019 period over India (Quaas et al., 2022). The increase in aerosol load might therefore exert a cooling influence that offsets part of the greenhouse gas warming. Moreover, India is generally greening (Kuttippurath & Kashyap, 2023) and changing land use and land cover can increase heavy rainfall events (Boyaj et al., 2020); other studies suggest that climate change increases the frequency of extreme events and extreme rainfall (Easterling et al., 2000; Prathipati et al., 2019). Clouds have a dual impact on surface temperature by suppressing or accelerating the trends. Banerjee et al., 2022, found that the clouds' impact on surface temperature in India is season dependent and changes between day and night.

This cooling trend is also seen in central and east Africa. In warm tropical environments, (Hegerl et al., 2007) reported an increase in the frequency and intensity of extreme rainfall events. In East Africa, drought under different climate scenarios follow the paradigm "dry get drier and wet gets wetter" with decreasing drought and skin temperatures particularly recorded in Kenya, Uganda, and Ethiopian highlands (Haile et al., 2020; Yang et al., 2019). In the Southern Pacific, close to the South America, negative Tskin/SST trends are observed in ERA5, IASI CDR, and IASI NN confined to/around the Humboldt Current System. Such localization strongly points to a wind-driven upwelling mechanism**,** as surface temperature in eastern boundary current systems is primarily controlled by alongshore winds, Ekman divergence, and the upwelling of cold subsurface waters. Strengthening of upwelling-favorable winds can therefore produce coastal cooling despite ongoing global ocean warming (Gutiérrez et al., 2011; Jebri et al., 2020). On the relatively short 2008–2022 period, internal Pacific decadal variability can further modulate these trends and project strongly onto the Peru–Chile upwelling region (Jebri et al., 2020).

The IASI-CDR shows more statistically significant trends, which is expected because the PWLR3 algorithm is a regression-based method. By design, it smooths short-term noise and inherits part of the temporal structure of its training dataset, producing a cleaner and more stable time series. As a result, long-term warming signals stand out more clearly, so more grid cells pass the significance test compared to fully independent retrievals, as IASI-NN dataset.

Panel (b) of Figure 6 summarizes the mean trends for the five products across land, sea and land+sea (globe) and for daytime and nighttime conditions separately. All trends are significant, except IASI-NN ones over sea. Results show predominantly positive trends, though their magnitudes vary by region and observing system. Land is heating at a much faster rate than the ocean (for all datasets). Over land, all five datasets report consistently positive trends with a very good agreement between MODIS, IASI-CDR, IASI-NN, and ERA5 during day with trends between +0.04 and +0.06. Daytime values range from +0.04 to +0.12, with CCI showing the strongest daytime trend. Nighttime trends range from +0.04 to +0.09, with IASI-CDR producing the largest positive trend and CCI the second one. Globally, IASI-CDR trends are higher than MODIS, ERA5 and IASI-NN ones.

https://doi.org/10.5194/egusphere-2026-400
Preprint. Discussion started: 11 February 2026

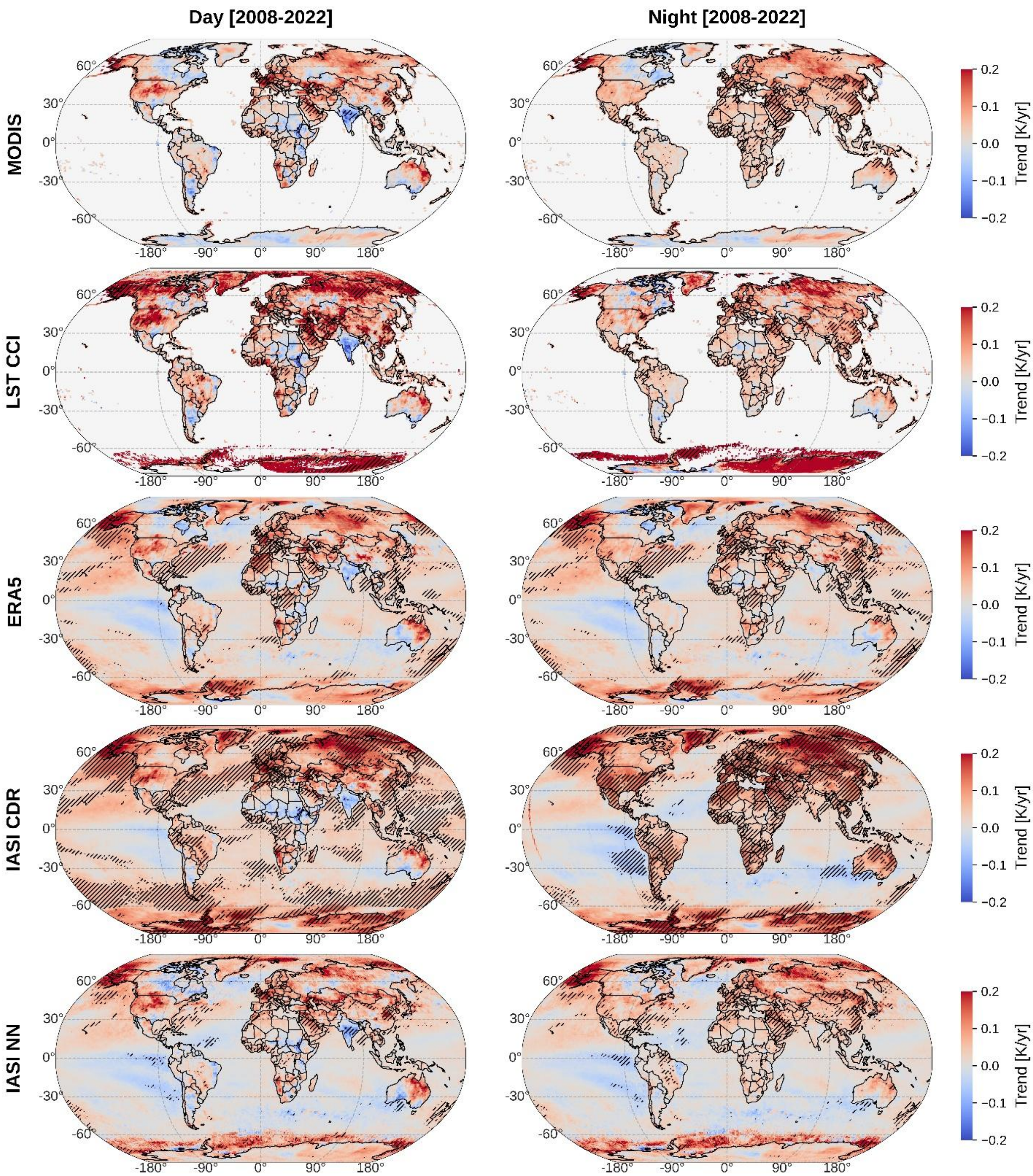

320 **(a)**

https://doi.org/10.5194/egusphere-2026-400
Preprint. Discussion started: 11 February 2026

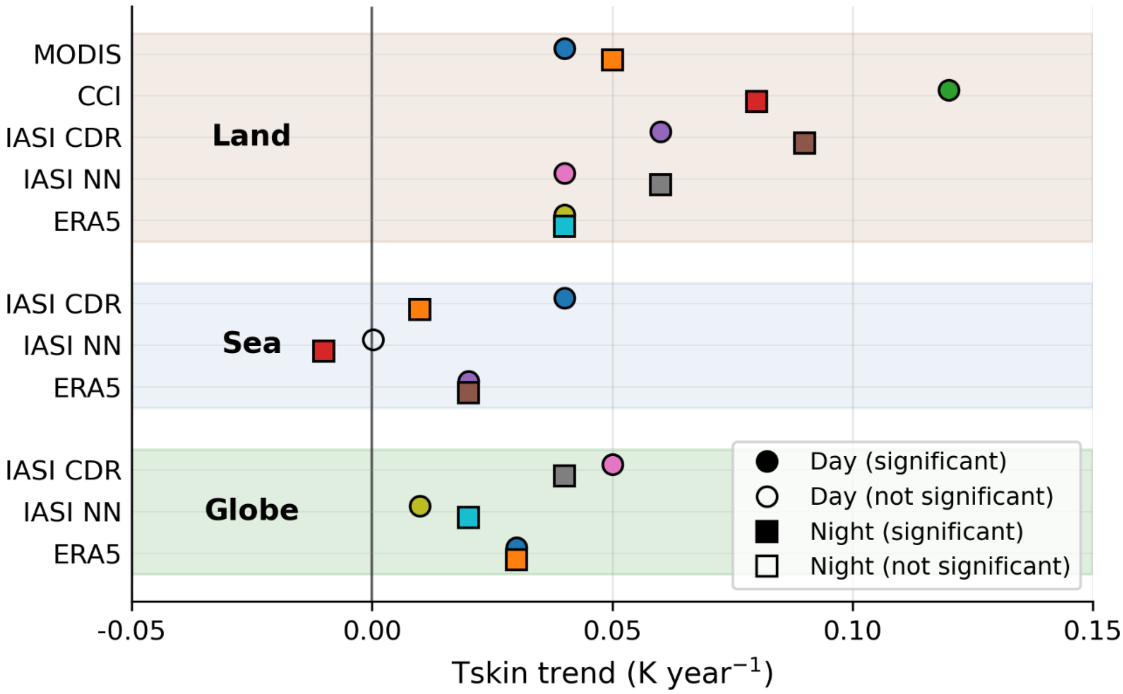

(b)

Figure 6. (a) Spatial trends [°K/year] during day (left column) and night (right column) for MODIS, LST CCI, ERA5, IASI-CDR, and IASI-NN over the period January 2008-December 2022. Stipples correspond to regions where trends are significant according to the standard Mann-Kendall test (p-value < 0.05). (b) Regional LST/Tskin trends (°K/yr) from MODIS, CCI LST, IASI-CDR, IASI-NN and ERA5 over the period [January 2008–December 2022]. Trends are computed with the Theil–Sen estimator on annual latitude-weighted and deseasonalised averages. Unfilled markers represent non-significant trends.

In the supplement, Figure S2, we show the latitude-dependent LST and SST trends (K/yr) during day and night from the different datasets. Trends are averaged over all the longitudes and spatially weighted by cos(latitude). The trends reveal a broadly consistent latitudinal structure across all datasets. Over land, daytime and nighttime trends generally increase toward the Northern Hemisphere and at high northern and southern latitudes, the effect of the Arctic amplification is clear across all datasets. MODIS, ERA5, IASI CDR, and IASI NN show close agreement across most latitudes, while the LST CCI product diverges most strongly in the Southern Hemisphere high latitudes. Over the oceans, SST trends are more uniform across datasets, with some divergences at mid and high northern latitudes.

Conclusions and discussions

In this study, we demonstrate how thermal infrared remote sensing can be used to monitor the evolution of Earth's skin temperature (Tskin)—over both land and ocean, and separately for morning and evening overpasses—using a suite of complementary observing systems over 2008–2022. We intercompared MODIS Terra LST (v6.1), ERA5 skin temperature, the latest ESA LST CCI product (v3.00), and two independent IASI-based retrievals: the EUMETSAT all-sky Climate Data Record (IASI-CDR, PWLR3) and a newly developed clear-sky neural-network product (IASI-NN). All datasets were harmonized to comparable local times (~09:30–10:30) and a common 1°×1° grid to assess each of the dataset consistency,

https://doi.org/10.5194/egusphere-2026-400
Preprint. Discussion started: 11 February 2026

anomalies/variability, and spatial trends. This work provides the first global, diurnally consistent intercomparison that simultaneously includes (1) the newly updated IASI-NN clear-sky product, (2) the homogeneously reprocessed IASI-CDR, and (3) the most recent ESA LST CCI v3.00 dataset, as well as MODIS and ERA5 products. Importantly, we assess day–night behaviour consistently across these datasets and across both land and ocean, enabling evaluation of the diurnal fingerprint of recent climate change from different datasets.

Over land, daytime global means agree within ~2 K across datasets, and deseasonalised anomalies are highly consistent, indicating that the major modes of interannual variability are robustly captured. However, two systematic caveats affect absolute values and, potentially, trends. First, LST CCI v3.00 exhibits step changes at sensor transitions (AATSR → MODIS Terra → SLSTR-B), visible in anomalies and reflected in larger RMSE. These discontinuities indicate residual inhomogeneities that must be considered when using v3.00. Second, MODIS Terra shows a pervasive nighttime cold bias relative to all other products, including LST CCI (which ingests MODIS radiances but applies a distinct retrieval chain). The magnitude and spatial extent of the MODIS nighttime bias are larger than expected from small overpass-time differences alone, which might be explained with known sensitivities of MODIS LST to cloud screening and residual cloud contamination (Gallo & Krishnan, 2022; Williamson et al., 2013), as well as reported cold biases at high latitudes (Muster et al., 2015; Østby et al., 2014) and at in situ validation sites (Tan et al., 2021).
IASI-NN (clear-sky) is systematically warmer than all-sky products (IASI-CDR, ERA5), particularly over land and at high latitudes, consistent with the well-documented "clear-sky bias" whereby averages computed from clear-sky satellite retrievals differ from true all-weather surface conditions (Ermida et al., 2019).
Over the ocean, inter-dataset biases are smaller than over land and generally remain below 1 K, with RMSE near ~1 K. Discrepancies increase toward high latitudes, where cloud detection, sea-ice contamination, and reduced thermal contrast degrade infrared retrieval sensitivity (Whitburn et al., 2022).

Spatial trend patterns over 2008–2022 are broadly consistent across datasets. All products show predominantly positive trends, stronger over land than ocean, and a clear signature of Arctic amplification at high northern latitudes, consistent with established evidence from observations and assessments (Masson-Delmotte et al., 2021). At regional scales, we robustly detect coherent areas of daytime cooling (e.g., India) and localized cooling in eastern boundary upwelling regions (e.g., the Peru–Chile/Humboldt system). The India signal is consistent with a combination of aerosol forcing, cloud radiative effects, and land-surface changes modulating the diurnal response (Banerjee et al., 2022; Klimont et al., 2013; Quaas et al., 2022; Wang et al., 2021). The southeastern Pacific cooling is physically consistent with wind-driven upwelling dynamics and modulation by internal decadal variability (Gutiérrez et al., 2011; Jebri et al., 2020). Over the sea, differences in trend magnitude remain dataset-dependent echoing recent findings that satellite-era SST trend estimates can differ consequentially across datasets (Menemenlis et al., 2025). Our results emphasize that uncertainty in surface temperature trends remains non-negligible and must be explicitly accounted for when using observations to constrain climate change.

This work illustrates the strong complementarity between different thermal infrared sensors and model-based products for characterising climate variability in Tskin. With the current IASI constellation (including IASI-C) expected to operate at least until 2030, and the continuity ensured by the IASI-New Generation series launched in 2025 with an intended lifetime extending to around 2045, long and internally consistent Tskin time series will continue to grow in length and quality. This will open new opportunities for global and regional monitoring of climate change at different times of the day from space.

Data Availability Statement

- IASI Artificial Neural Network skin temperature data: Metop A: https://doi.org/10.21413/iasi-ft_metopa_skt_l3_latmos-ulb and Metop B: https://doi.org/10.21413/iasi-ft_metopb_skt_l3_latmos-ulb (Safieddine, S., 2026)
- IASI EUMETSAT all sky data product: https://doi.org/10.15770/EUM_SEC_CLM_0063 (EUMETSAT, 2022)
- The Modis TERRA MOD11C3 Version 6.1 LST data can be accessed through NASA's LP DAAC data portal: https://doi.org/10.5067/MODIS/MOD11C3.061 (Wan Z., et al, 2021)
- ERA5 Tskin is available at the climate data store: https://doi.org/10.24381/cds.f17050d7 (Copernicus Climate Change Service, 2023)
- LST CCI V3.00 is available at: https://dx.doi.org/10.5285/e67b02b814bf4a78b9ec90b4259f0741 (Ghent et al., 2025)

Annex. Channels used to retrieve skin temperature from IASI (in order of Tskin information content):

1300,1282,1249,1272,1254,1294,1230,1164,1267,1194,1179,1222,1311,1086,1157,1172,1142,1203,1018,1141,1009,1089,1115,1025,1126,1038,1100,1001,1321,1209,1069,997,1070,921,962,1051,940,916,1114,950,869,1237,926,961,875,979,889,899,897,1052,853,984,862,771,759,752,797,745,775,801,714,706,698,844,726,810,736,824,691,669,661,786,827,642,650,682,582,630,625,574,584,547,551,565,534,619,521

Author contribution:

SS and SS generated the figures and prepared the manuscript with contributions from all co-authors. . JHL made available IASI EUMETSAT all sky data to co-authors. MDB provided input on the Tskin CDR, SW and LC provided input on the cloud cover used to generate the Tskin NN dataset. CC secured the funding. All authors reviewed the manuscript.

Acknowledgments

The IASI mission is a joint mission of Eumetsat and the Centre National d'Etudes Spatiales (CNES, France). The IASI L1 data are distributed in near real time by Eumetsat through the Eumetcast system distribution. The authors acknowledge the Aeris data infrastructure for providing the IASI L1C data.
This project has received funding from the European Research Council (ERC) under the European Union's Horizon 2020 and innovation programme (grant agreement No 742909).

References

Banerjee, A. K., Dutta, S., & Dey, S. (2022). Contrasting impacts of net cloud radiative forcing on the surface temperature trends in India. *Environmental Research Communications*, *4*(4), 041005. https://doi.org/10.1088/2515-7620/ac52e0

https://doi.org/10.5194/egusphere-2026-400
Preprint. Discussion started: 11 February 2026

Bouillon, M., Safieddine, S., Hadji-Lazaro, J., Whitburn, S., Clarisse, L., Doutriaux-Boucher, M., Coppens, D., August, T., Jacquette, E., & Clerbaux, C. (2020). Ten-Year Assessment of IASI Radiance and Temperature. *Remote Sensing*, *12*(15), Article 15. https://doi.org/10.3390/rs12152393

Boyaj, A., Dasari, H. P., Hoteit, I., & Ashok, K. (2020). Increasing heavy rainfall events in south India due to changing land use and land cover. *Quarterly Journal of the Royal Meteorological Society*, *146*(732), 3064–3085. https://doi.org/10.1002/qj.3826

Clerbaux, C., Boynard, A., Clarisse, L., George, M., Hadji-Lazaro, J., Herbin, H., Hurtmans, D., Pommier, M., Razavi, A., Turquety, S., Wespes, C., & Coheur, P.-F. (2009). Monitoring of atmospheric composition using the thermal infrared IASI/MetOp sounder. *Atmospheric Chemistry and Physics*, *9*(16), 6041–6054. https://doi.org/10.5194/acp-9-6041-2009

Copernicus Climate Change Service. (2023). *ERA5 monthly averaged data on single levels from 1940 to present. Copernicus Climate Change Service (C3S) Climate Data Store (CDS)* [Dataset]. https://doi.org/10.24381/cds.f17050d7

Easterling, D. R., Meehl, G. A., Parmesan, C., Changnon, S. A., Karl, T. R., & Mearns, L. O. (2000). Climate Extremes: Observations, Modeling, and Impacts. *Science*, *289*(5487), 2068–2074. https://doi.org/10.1126/science.289.5487.2068

Ermida, S. L., Trigo, I. F., DaCamara, C. C., Jiménez, C., & Prigent, C. (2019). Quantifying the Clear-Sky Bias of Satellite Land Surface Temperature Using Microwave-Based Estimates. *Journal of Geophysical Research: Atmospheres*, *124*(2), 844–857. https://doi.org/10.1029/2018JD029354

EUMETSAT. (2022). *IASI All Sky Temperature and Humidity Profiles—Climate Data Record Release 1.1—Metop-A and -B, European Organisation for the Exploitation of Meteorological Satellites* [netCDF4]. 10.15770/EUM_SEC_CLM_0063. https://doi.org/10.15770/EUM_SEC_CLM_0063

Gallo, K., & Krishnan, P. (2022). Evaluation of the Bias in the Use of Clear-Sky Compared with All-Sky Observations of Monthly and Annual Daytime Land Surface Temperature. *Journal of Applied Meteorology and Climatology*, *61*(10), 1485–1495. https://doi.org/10.1175/JAMC-D-21-0240.1

Ghent, D., Veal, K., & Perry, M. (2025). *ESA Land Surface Temperature Climate Change Initiative (LST_cci): Daily multisensor Infra-Red (IR) Low Earth Orbit (LEO) land surface temperature (LST) time series level 3 supercollated (L3S) global product (1995-2024), version 3.00* (p. 20258 Files, 5001176579070 B) [Application/xml]. NERC EDS Centre for Environmental Data Analysis. https://doi.org/10.5285/E67B02B814BF4A78B9EC90B4259F0741

Guillevic, P., Göttsche, F., Nickeson, J., Hulley, G., Ghent, D., Yu, Y., Trigo, I., Hook, S., Sobrino, J. A., Remedios, J., Román, M., & Camacho, F. (2018). *Land Surface Temperature Product Validation Best Practice Protocol Version 1.1—January, 2018*. https://doi.org/10.5067/doc/ceoswgcv/lpv/lst.001

Gutiérrez, D., Bouloubassi, I., Sifeddine, A., Purca, S., Goubanova, K., Graco, M., Field, D., Méjanelle, L., Velazco, F., Lorre, A., Salvatteci, R., Quispe, D., Vargas, G., Dewitte, B., & Ortlieb, L. (2011). Coastal cooling and increased productivity in the main upwelling zone off Peru since the mid-twentieth century. *Geophysical Research Letters*, *38*(7). https://doi.org/10.1029/2010GL046324

Hachem, S., Duguay, C. R., & Allard, M. (2012). Comparison of MODIS-derived land surface temperatures with ground surface and air temperature measurements in continuous permafrost terrain. *The Cryosphere*, *6*(1), 51–69. https://doi.org/10.5194/tc-6-51-2012

Haile, G. G., Tang, Q., Hosseini-Moghari, S.-M., Liu, X., Gebremicael, T. G., Leng, G., Kebede, A., Xu, X., & Yun, X. (2020). Projected Impacts of Climate Change on Drought Patterns Over East Africa. *Earth's Future*, *8*(7), e2020EF001502. https://doi.org/10.1029/2020EF001502

Hegerl, G. C., Crowley, T. J., Allen, M., Hyde, W. T., Pollack, H. N., Smerdon, J., & Zorita, E. (2007). Detection of Human Influence on a New, Validated 1500-Year Temperature Reconstruction. *Journal of Climate*, *20*(4), 650–666. https://doi.org/10.1175/JCLI4011.1

Hersbach, H., Bell, B., Berrisford, P., Hirahara, S., Horányi, A., Muñoz-Sabater, J., Nicolas, J., Peubey, C., Radu, R., Schepers, D., Simmons, A., Soci, C., Abdalla, S., Abellan, X., Balsamo, G., Bechtold, P., Biavati, G., Bidlot, J., Bonavita, M., … Thépaut, J.-N. (2020). The ERA5 global reanalysis. *Quarterly Journal of the Royal Meteorological Society*, *146*(n/a), 1999–2049. https://doi.org/10.1002/qj.3803

https://doi.org/10.5194/egusphere-2026-400
Preprint. Discussion started: 11 February 2026

Hulley, G. C., Ghent, D., Göttsche, F. M., Guillevic, P. C., Mildrexler, D. J., & Coll, C. (2019). 3—Land Surface Temperature. In G. C. Hulley & D. Ghent (Eds.), *Taking the Temperature of the Earth* (pp. 57–127). Elsevier. https://doi.org/10.1016/B978-0-12-814458-9.00003-4

Jebri, B., Khodri, M., Echevin, V., Gastineau, G., Thiria, S., Vialard, J., & Lebas, N. (2020). Contributions of Internal Variability and External Forcing to the Recent Trends in the Southeastern Pacific and Peru–Chile Upwelling System. *Journal of Climate*, *33*(24), 10555–10578. https://doi.org/10.1175/JCLI-D-19-0304.1

Kedall, M. G. (1970). *Rank Correlation Methods. Fourth Edition*. https://www.abebooks.com/Rank-Correlation-Methods-Fourth-Edition-Maurice/1243973521/bd

Khadka, A., Wagnon, P., Brun, F., Shrestha, D., Lejeune, Y., & Arnaud, Y. (2022). Evaluation of ERA5-Land and HARv2 Reanalysis Data at High Elevation in the Upper Dudh Koshi Basin (Everest Region, Nepal). *Journal of Applied Meteorology and Climatology*, *61*(8), 931–954. https://doi.org/10.1175/JAMC-D-21-0091.1

Kilymis, D., Kangah, Y., Le Barbier, L., Jacquette, E., Lenot, X., Ansart, J., Faillot, M., Calvel, J.-C., Codou, G., & Vandermarcq, O. (2025). IASI global radiometric uncertainty budget. *Atmospheric Measurement Techniques*, *18*(21), 6513–6525. https://doi.org/10.5194/amt-18-6513-2025

Klimont, Z., Smith, S. J., & Cofala, J. (2013). The last decade of global anthropogenic sulfur dioxide: 2000–2011 emissions. *Environmental Research Letters*, *8*(1), 014003. https://doi.org/10.1088/1748-9326/8/1/014003

Kuttippurath, J., & Kashyap, R. (2023). Greening of India: Forests or Croplands? *Applied Geography*, *161*, 103115. https://doi.org/10.1016/j.apgeog.2023.103115

Liu, Z.-H., Weng, S.-S., Zeng, Z.-L., Ding, M.-H., Wang, Y.-Q., & Liang, Z. (2024). Hourly land surface temperature retrieval over the Tibetan Plateau using Geo-LightGBM framework: Fusion of Himawari-8 satellite, ERA5 and site observations. *Advances in Climate Change Research*, *15*(4), 623–635. https://doi.org/10.1016/j.accre.2024.06.007

Mann, H. B. (1945). Nonparametric Tests Against Trend. *Econometrica*, *13*(3), 245–259. https://onlinelibrary.wiley.com/doi/abs/0012-9682(194507)13:3<245:NTAT>2.0.CO;2-U

Masson-Delmotte, V., P. Zhai, A. Pirani, S.L., Connors, C. Péan, S. Berger, N. Caud, Y. Chen, L. Goldfarb, M.I. Gomis, M. Huang, K. Leitzell, E. Lonnoy, J.B.R., & Matthews, T.K. Maycock, T. Waterfield, O. Yelekçi, R. Yu, and B. Zhou.

https://doi.org/10.5194/egusphere-2026-400
Preprint. Discussion started: 11 February 2026

(2021). *IPCC, 2021: Climate Change 2021: The Physical Science Basis. Contribution of Working Group I to the Sixth Assessment Report of the Intergovernmental Panel on Climate Change*. Cambridge University Press. In Press. https://www.ipcc.ch/assessment-report/ar6/

Menemenlis, S., Vecchi, G. A., Yang, W., Fueglistaler, S., & Raghuraman, S. P. (2025). Consequential differences in satellite-era sea surface temperature trends across datasets. *Nature Climate Change*, *15*(8), 897–903. https://doi.org/10.1038/s41558-025-02362-6

Muster, S., Langer, M., Abnizova, A., Young, K. L., & Boike, J. (2015). Spatio-temporal sensitivity of MODIS land surface temperature anomalies indicates high potential for large-scale land cover change detection in Arctic permafrost landscapes. *Remote Sensing of Environment*, *168*, 1–12. https://doi.org/10.1016/j.rse.2015.06.017

Østby, T. I., Schuler, T. V., & Westermann, S. (2014). Severe cloud contamination of MODIS Land Surface Temperatures over an Arctic ice cap, Svalbard. *Remote Sensing of Environment*, *142*, 95–102. https://doi.org/10.1016/j.rse.2013.11.005

Prathipati, V. K., Naidu, C. V., & Konatham, P. (2019). Inconsistency in the frequency of rainfall events in the Indian summer monsoon season. *International Journal of Climatology*, *39*(13), 4907–4923. https://doi.org/10.1002/joc.6113

Quaas, J., Jia, H., Smith, C., Albright, A. L., Aas, W., Bellouin, N., Boucher, O., Doutriaux-Boucher, M., Forster, P. M., Grosvenor, D., Jenkins, S., Klimont, Z., Loeb, N. G., Ma, X., Naik, V., Paulot, F., Stier, P., Wild, M., Myhre, G., & Schulz, M. (2022). Robust evidence for reversal of the trend in aerosol effective climate forcing. *Atmospheric Chemistry and Physics*, *22*(18), 12221–12239. https://doi.org/10.5194/acp-22-12221-2022

Rhee, J., Im, J., & Carbone, G. J. (2010). Monitoring agricultural drought for arid and humid regions using multi-sensor remote sensing data. *Remote Sensing of Environment*, *114*(12), 2875–2887. https://doi.org/10.1016/j.rse.2010.07.005

Safieddine, S., Clerbaux, C., Muñoz-Sabater, J., & Thépaut, J.-N. (2025). Local hourly trends in near-surface and land surface temperatures. *Scientific Reports*, *15*(1), 29915. https://doi.org/10.1038/s41598-025-15731-0

https://doi.org/10.5194/egusphere-2026-400
Preprint. Discussion started: 11 February 2026

Safieddine, S., Parracho, A. C., George, M., Aires, F., Pellet, V., Clarisse, L., Whitburn, S., Lezeaux, O., Thépaut, J.-N., Hersbach, H., Radnoti, G., Göettsche, F.-M., Martin, M. A., Doutriaux-Boucher, M., Coppens, D., August, T., Zhou, D. K., & Clerbaux, C. (2020). Artificial Neural Networks to Retrieve Land and Sea Skin Temperature from IASI. *Remote Sensing*, *12*(17), Article 17. https://doi.org/10.3390/rs12172777

Sarah Safieddine. (2026). *IASI-FT Skin Temperature (from IASI/Metop-A, B and C)* [Dataset]. https://doi.org/Metop%2520A:%2520https://doi.org/10.21413/iasi-ft_metopa_skt_l3_latmos-ulb%2520and%2520Metop%2520B:%2520https://doi.org/10.21413/iasi-ft_metopb_skt_l3_latmos-ulb

Sen, P. K. (1968). Estimates of the Regression Coefficient Based on Kendall's Tau. *Journal of the American Statistical Association*, *63*(324), 1379–1389. https://doi.org/10.1080/01621459.1968.10480934

Tan, J., Che, T., Wang, J., Liang, J., Zhang, Y., & Ren, Z. (2021). Reconstruction of the Daily MODIS Land Surface Temperature Product Using the Two-Step Improved Similar Pixels Method. *Remote Sensing*, *13*(9), 1671. https://doi.org/10.3390/rs13091671

Tchebakova, N. M., Parfenova, E., & Soja, A. J. (2009). The effects of climate, permafrost and fire on vegetation change in Siberia in a changing climate. *Environmental Research Letters*, *4*(4), 045013. https://doi.org/10.1088/1748-9326/4/4/045013

Theil, H. (1992). A Rank-Invariant Method of Linear and Polynomial Regression Analysis. In B. Raj & J. Koerts (Eds.), *Henri Theil's Contributions to Economics and Econometrics: Econometric Theory and Methodology* (pp. 345–381). Springer Netherlands. https://doi.org/10.1007/978-94-011-2546-8_20

Wan, Z., Hook, S., Hulley, G. (2021). *MODIS/Terra Land Surface Temperature/Emissivity Monthly L3 Global 0.05Deg CMG V061 [Data set]* [Dataset]. https://doi.org/10.5067/MODIS/MOD11C3.061

Wang, Z., Lin, L., Xu, Y., Che, H., Zhang, X., Zhang, H., Dong, W., Wang, C., Gui, K., & Xie, B. (2021). Incorrect Asian aerosols affecting the attribution and projection of regional climate change in CMIP6 models. *Npj Climate and Atmospheric Science*, *4*(1), Article 1. https://doi.org/10.1038/s41612-020-00159-2

https://doi.org/10.5194/egusphere-2026-400
Preprint. Discussion started: 11 February 2026

Whitburn, S., Clarisse, L., Crapeau, M., August, T., Hultberg, T., Coheur, P. F., & Clerbaux, C. (2022). A CO_2-independent cloud mask from Infrared Atmospheric Sounding Interferometer (IASI) radiances for climate applications. *Atmospheric Measurement Techniques*, *15*(22), 6653–6668. https://doi.org/10.5194/amt-15-6653-2022

Williamson, S. N., Hik, D. S., Gamon, J. A., Kavanaugh, J. L., & Koh, S. (2013). Evaluating Cloud Contamination in Clear-Sky MODIS Terra Daytime Land Surface Temperatures Using Ground-Based Meteorology Station Observations. *Journal of Climate*, *26*(5), 1551–1560. https://doi.org/10.1175/JCLI-D-12-00250.1

Yang, T., Ding, J., Liu, D., Wang, X., & Wang, T. (2019). Combined Use of Multiple Drought Indices for Global Assessment of Dry Gets Drier and Wet Gets Wetter Paradigm. *Journal of Climate*, *32*(3), 737–748. https://doi.org/10.1175/JCLI-D-18-0261.1

Yoo, C., Im, J., Cho, D., Lee, Y., Bae, D., & Sismanidis, P. (2022). Downscaling MODIS nighttime land surface temperatures in urban areas using ASTER thermal data through local linear forest. *International Journal of Applied Earth Observation and Geoinformation*, *110*, 102827. https://doi.org/10.1016/j.jag.2022.102827

Zhai, Z., Wang, Y., Reijmer, C. H., Smeets, P. C. J. P., Zhang, X., & Zhang, W. (2024). MODIS land surface temperature in East Antarctica: Accuracy and its main affecting factors. *Journal of Glaciology*, *70*, e22. https://doi.org/10.1017/jog.2024.17

Zhou, L., Dickinson, R. E., Tian, Y., Jin, M., Ogawa, K., Yu, H., & Schmugge, T. (2003). A sensitivity study of climate and energy balance simulations with use of satellite-derived emissivity data over Northern Africa and the Arabian Peninsula. *Journal of Geophysical Research: Atmospheres*, *108*(D24). https://doi.org/10.1029/2003JD004083